CHEMISTRY OF MATERIALS

pubs.acs.org/cm

Article

Branched Fluorenylidene Derivatives with Low Ionization Potentials as Hole-Transporting Materials for Perovskite Solar Cells

Aistė Jegorovė,[†] Jianxing Xia,[†] Matas Steponaitis, Maryte Daskeviciene, Vygintas Jankauskas, Alytis Gruodis, Egidijus Kamarauskas, Tadas Malinauskas, Kasparas Rakstys, Khalid A. Alamry, Vytautas Getautis,* and Mohammad Khaja Nazeeruddin*

Cite This: *Chem. Mater.* 2023, 35, 5914–5923

Read Online

ACCESS | Metrics & More | Article Recommendations | Supporting Information

ABSTRACT: A group of small-molecule hole-transporting materials (HTMs) that are based on fluorenylidene fragments were synthesized and tested in perovskite solar cells (PSCs). The investigated compounds were synthesized by a facile two-step synthesis, and their properties were measured using thermoanalytical, optoelectronic, and photovoltaic methods. The champion PSC device that was doped with lithium bis(trifluoromethanesulfonyl)imide (LiTFSI) reached a power conversion efficiency of 22.83%. The longevity of the PSC device with the best performing HTM, **V1387**, was evaluated in different conditions and compared to that of 2,2′,7,7′-tetrakis(*N*,*N*-di-*p*-methoxyphenylamine)-9,9′-spirobifluorene (spiro-MeOTAD), showing improved stability. This work provides an alternative HTM strategy for fabricating efficient and stable PSCs.

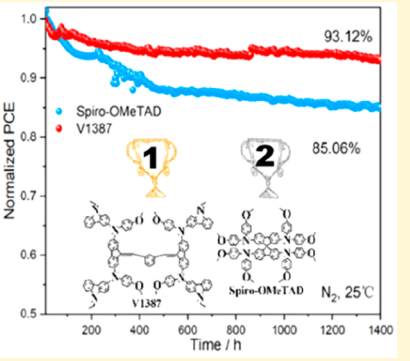

1. INTRODUCTION

Since the naming of the first perovskite in the 19th century,[1] various materials have been discovered and described as perovskites.[2−4] These materials can be organic,[5] inorganic,[6] or hybrid.[7] With a few exceptions, perovskites are generalized with the formula ABX_3, where A and B are cations of different charges (mono- and dications) and X is an anion that coordinates B. The recent attention of perovskite materials for use in optoelectronics should come as no surprise, as they have large absorption coefficients, tunable compositions and absorption edges, long charge carrier diffusion lengths, high defect tolerances, and efficient charge transport properties.[8,9] Furthermore, perovskites can be processed in a variety of different ways,[10−13] making them attractive not only for research but also for potential commercial applications.[14,15]

One of the most researched topics in science is the study of perovskite solar cells (PSCs). Since the first article published in 2009, the efficiency of PSCs has skyrocketed from 3.8% to over 26%.[16] However, the rapid emergence of PSCs does not mean the technology has no flaws. Unsolved fabrication issues, unstable charge-transporting materials, and the long-term stability of perovskite compositions and devices must be addressed before this technology can reach the market. Additionally, using a quality hole-transporting material (HTM) is crucial for creating efficient and stable PSC devices.[17,18] The function of an HTM is to efficiently transport photogenerated positive carriers from the absorber to the electrode. To achieve this, the HTM has to be chemically and morphologically stable, have the appropriate energy levels, and have a relatively high carrier mobility.[19] Over the years, efficiency records have mostly been broken by devices using either 2,2′,7,7′-tetrakis(*N*,*N*-di-*p*-methoxyphenylamine)-9,9′-spirobifluorene (spiro-MeOTAD) or poly[bis(4-phenyl)-(2,4,6-trimethylphenyl)amine] (PTAA) as an HTM. However, these materials are expensive and relatively difficult to synthesize, and spiro-MeOTAD is known to have stability issues.[20−23] In order to replace spiro-MeOTAD, researchers have synthesized many new molecules with the same "award winning" structural design,[24−26,26] hoping to achieve higher power conversion efficiencies (PCEs). Various polymers have also been developed in an attempt to replace PTAA as an HTM.[27−30] To mimic spiro-MeOTAD, there are two commonly used strategies: (1) keep the central spiro core and only change the substituents around it[31−33] or (2) build a molecule by carefully choosing substituents around a chosen central core in order to imitate the spatial arrangement of spiro-MeOTAD.[34−36] Early on in the research of PSCs, the first strategy proved more fruitful, successfully creating PSCs with higher PCEs. The second strategy then became more

Received: March 29, 2023
Revised: July 11, 2023
Published: July 29, 2023

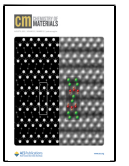

Scheme 1. Synthesis of the HTMs V1322, V1387, V1391, V1424, V1388, and V1389

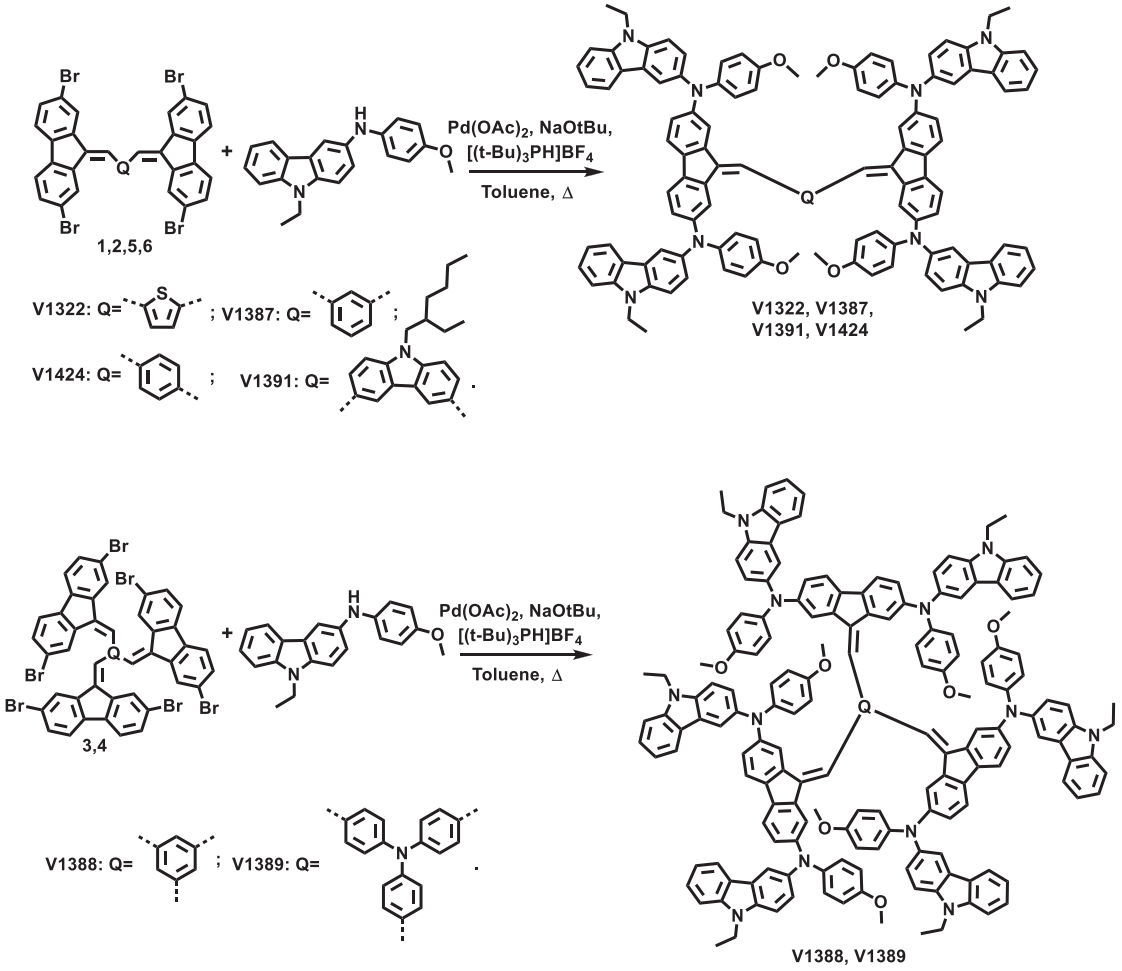

popular later on, when the cost and stability of PSC devices became factors that needed to be addressed.

In one of our previous works, we demonstrated that using HTMs based on methoxydiphenylamine-substituted fluorene derivatives with a small central core is a good strategy for fabricating highly efficient PSCs.[37] To expand on our aforementioned study, we decided to employ carbazole-containing substituents as electron donating units, as this is known to tune the highest occupied molecular orbital (HOMO) level and help reach a high PCE.[38−40] Furthermore, carbazole is a suitable building block for HTMs due to the possibility of having numerous substitutions of the carbazole unit. Various carbazole-containing scaffolds as electron donating units were used in order to tune the energy levels of HTMs, showing a good photovoltaic performance. For example, SGT series,[41,42] benzodithiazole-,[43] bipyridine-,[44] and pyrene-based[45] electron donating units were used to fabricate highly efficient devices.

In this work, we describe the synthesis and application of new HTMs comprised of various central core units and substituted carbazole derivatives. These materials can be obtained in a facile two-step synthesis procedure. Their thermal, optical, and photoelectrical properties were also thoroughly investigated. All of the tested novel HTMs were successfully applied in PSCs, reaching an efficiency of up to 22%. Furthermore, the device employing the best performing HTM, **V1387**, demonstrated improved long-term stability compared to PSCs that use spiro-MeOTAD as a *p*-type charge carrier.

2. RESULTS AND DISCUSSION

All of the newly synthesized HTMs can be divided into two groups: molecules with two fluorene units in their central core structure and molecules with three fluorene units. Compounds **1**−**6** were synthesized by a base-catalyzed condensation reaction; an example of said reaction can be seen in Scheme S1. All HTMs were obtained by palladium cross-coupling reactions between the respective central core unit and 9-ethyl-*N*-(4-metoxyphenyl)-9*H*-carbazol-3-amine (Scheme 1). Detailed synthetic protocols of said materials are described in the Supporting Information.

To determine the thermal and morphological stability of the HTMs, thermogravimetric analysis (TGA) and differential scanning calorimetry (DSC) were used. Analysis of the TGA data suggests that all HTMs decompose around 450 °C (Figure 1), far above the temperature required for conventional device operation.[14] DSC measurements reveal that the new organic semiconductors are molecular glasses having glass transition temperatures (T_g) between 190 and 232 °C (Figure S1), surpassing the T_g of spiro-MeOTAD (124 °C).[46] This suggests that our new materials are more morphologically stable.

Quantum chemistry simulations of the ground state molecular structures for several of the most probable

https://doi.org/10.1021/acs.chemmater.3c00708
Chem. Mater. 2023, 35, 5914−5923

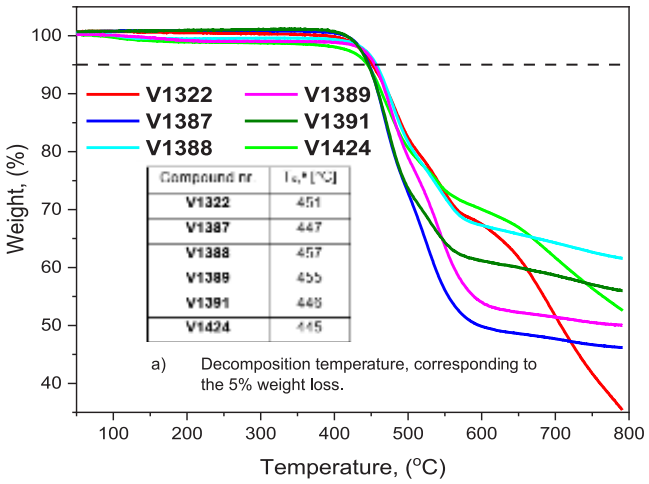

Figure 1. TGA curves of the synthesized HTMs.

conformers were provided using Gaussian 16[47] software by means of density functional theory (DFT) via the B3LYP method and a 6-31G(d) basis set, supplemented with polarization functions (d). Solvation effects were not considered in all cases. A list of several of the most probable molecular conformations is presented in Table S2. Two projections (*xy* and *xz*) of each of the mentioned conformations are presented in Figures S5−S10. In all cases, it is necessary to point out that the molecular structures are presented in a chaotic manner due to the absence of total or partial symmetry and the existence of a very large number of different conformers. All presented structures in Table S2 were obtained using a gradient optimization technique (convergence of the maximum force, root mean square (RMS) force, maximum displacement, and RMS displacement parameters has been achieved). Electronic excitations were simulated using a semi-empirical temporal difference (TD) method (for singlets). The parameters of the electronic excitations (transition energies ΔE_1 ($S_0 \rightarrow S_1$) and ΔE_2 ($S_0 \rightarrow S_2$) and corresponding oscillator strengths f_1 and f_2) are presented in Table S7. The populations of the low lying excited molecular states S_1 and S_2 could be realized using forbidden transitions: $S_0 \rightarrow S_n$, where $n = 1$ and 2 (oscillator strengths $f_n \rightarrow 0$). In a condensed phase, due to close intermolecular contacts, this prohibition is partially removed. The parameters of the transition between the molecular orbitals (MOs), which are related to the population of the "spectroscopic" states S_n, (n = 1 and 2) are presented in Table S3. In all cases, the dominant and most significant electron jump exists between the HOMO and the lowest unoccupied molecular orbital (LUMO). The spatial distributions of electron density (for the HOMO−1, HOMO, LUMO, and LUMO+1 of each compound) are presented in Tables S4−S6. For **V1322**, the thiophene core plays an important role in establishing the charge redistribution between the center core (and partially the left substituent) and the right substituent (see Table S4). For **V1387**, the phenyl core (linked in positions 1 and 3 to two fluorene substituents) forms a unit that has a similar role: to establish the charge redistribution between the left and right substituents and the central core (see Table S4). For **V1391**, a central core is formed using carbazole with two linked fluorenes, and a core fragment takes part in the charge redistribution between the left and right substituents and the central core (see Table S5). For **V1424**, the phenyl core (linked in positions 1 and 4 to two fluorene substituents) forms a unit that has a similar role: to establish the charge redistribution between the left and right substituents and the central core (see Table S5). The formation of a central unit is more effective for **V1424** than in the case of **V1387**, due to the different link conditions. For **V1388**, the phenyl core (linked in positions 1, 3, and 5 to three fluorene substituents) forms a unit for establishing the charge redistribution between the left and right substituents and the central core (see Table S6). For **V1389**, a central unit is formed from triphenylamine (TPA), and the charge redistribution between the left and right substituents and the central core is established (see Table S6).

The ultraviolet−visible (UV−vis) absorption spectra of the V series HTMs were measured in a tetrahydrofuran (THF) solution and on glass substrates (Figure 2a,b). All of the compounds have two major absorption peaks at around 300 and 375 nm, which represent the $\pi-\pi^*$ transitions. The materials **V1322** and **V1389** both have an extra peak in the 450−470 nm range, which most likely corresponds to the $\pi-\pi^*$ transitions with some charge transfer character, owing to the electron-rich nature of triarylamine and thiophene π systems. When comparing the spectra of the same compounds

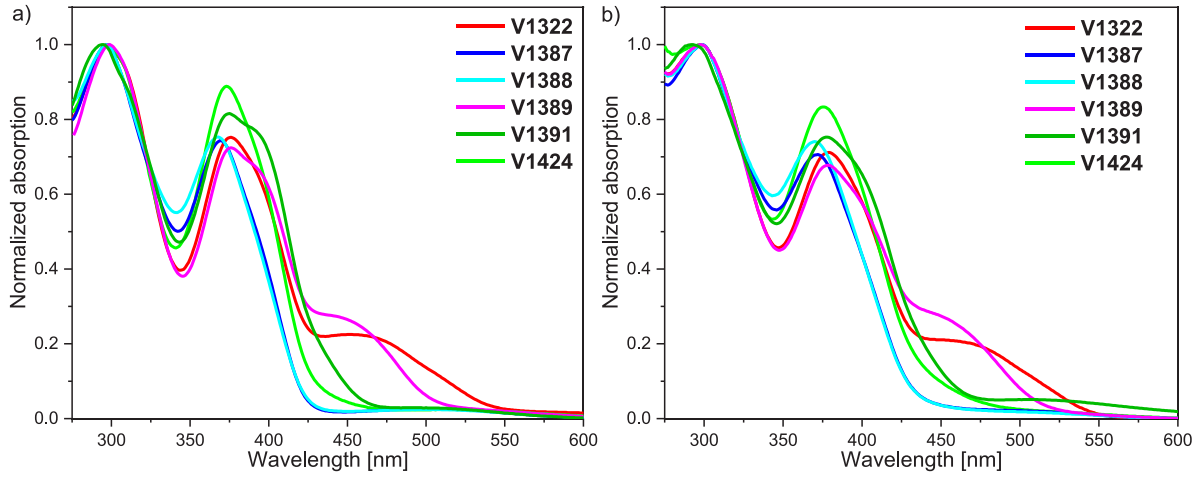

Figure 2. UV−vis absorption spectra of the V series HTMs (a) in a THF solution and (b) as thin films on glass substrates.

https://doi.org/10.1021/acs.chemmater.3c00708
Chem. Mater. 2023, 35, 5914−5923

in solution to those acting as thin films, practically no shift in absorption is observed.

To evaluate the energy levels of the synthesized materials in the solid state, the ionization potential (I_p) was measured by photoelectron spectroscopy in air (PESA), where the measurement error was evaluated to be 0.03 eV. The I_p values of the synthesized HTMs can be seen in Figure 3. All of the tested

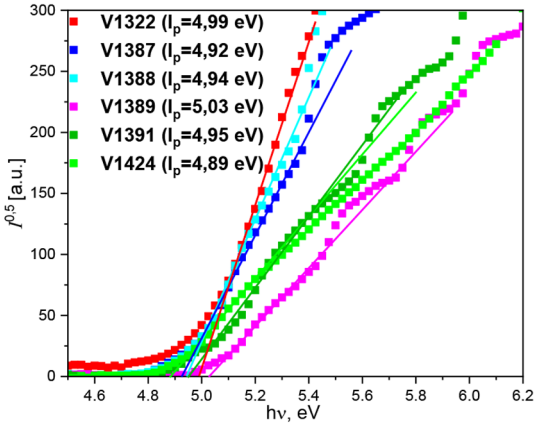

Figure 3. Ionization potential of the compounds **V1322**, **V1387**, **V1388**, **V1389**, **V1391**, and **V1424**.

materials have a relatively high HOMO energy level at ∼5.0 eV. After analyzing the data, it seems that the biggest influence on I_p is the central core rather than the number of substitutions around it. The HTMs that contain single phenyl rings in their core (**V1387**, **V1388**, and **V1424**) have the highest HOMO levels, while the HTMs that have carbazole, thiophene, and TPA central fragments have slightly lower energy levels. This minor difference in I_p could be the cause of slightly bulkier cores, which in turn causes more steric hindrance in the solid state.

Hole mobility was measured from thin films via the xerographic time-of-flight (XTOF) method, with the electric field dependencies of the hole drift mobilities shown in Figure 4. Due to poor layer formation, the investigated materials had to be mixed with bisphenol Z polycarbonate (PC-Z, weight ratio 1:1) in order to form uniform thin films, which are necessary for accurate drift carrier mobility evaluation. **V1424** had the highest zero-field hole mobility ($\mu_0 = 1.9 \times 10^{-6}$ cm^2 V^{-1} s^{-1}), while the mobility values for the other semi-

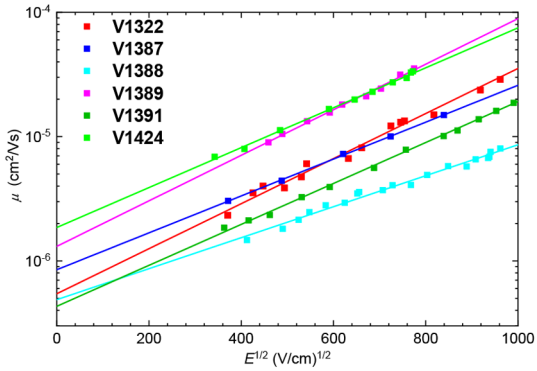

Figure 4. Charge carrier mobility of the V series HTMs, measured with PC-Z.

conductors were slightly lower. In comparison to spiro-MeOTAD ($\mu_0 = 1.3 \times 10^{-4}$ cm^2 V^{-1} s^{-1}),[48] these values are significantly lower. However, it is worth noting that results acquired from HTM mixtures with PC-Z are generally at least one order of magnitude lower than those of the pristine material. The thermal, optical, and photoelectrical properties of the new *p*-type semiconductors are summarized in Table 1.

Next, PSCs were prepared with the synthesized materials in a regular configuration (*n-i-p*). For each PSC, fluorinated tin oxide (FTO) was used as a front contact, SnO_2 and compact and mesoporous TiO_2 (c-TiO_2 and m-TiO_2, respectively) were used as the electron-transporting layers (ETLs), a triple cation perovskite was used as the light absorber, and the synthesized HTM was responsible for transporting positive charges toward the back contact, which in this case was gold (Figure 5a). Cross-sectional scanning electron microscopy (SEM) images of one of the devices can be seen in Figure 5b. Surface SEM was also used to study **V1387** on the perovskite layer. As compared with the bare perovskite film, the additional layer of **V1387** fully covered the perovskite crystal (Figure S2). The energy level illustration of various HTMs depicted in Figure 5c shows that all of the HTMs that were created in this study have around the same energy as spiro-OMeTAD; thus, they are suitable for hole transportation in PSCs.[49,50] Time-resolved photoluminescence (TRPL, Figure 5d) was performed on the glass/perovskite/**V1387** and glass/perovskite/spiro-OMeTAD films. The TRPL decay time was fitted by a bi-exponential model with fast (τ_1) and slow (τ_2) components, which indicate the interfacial transportation and recombination, respectively. The average decay time (τ_{ave}) is calculated using the equation $\tau_{ave} = \sum A_i\tau_i^2 / \sum A_i\tau_i$, where A_i and τ_i represent the decay amplitude and the decay time component, respectively (Table 2). For interfacial transport, the fast (τ_1) component was considered. When the spiro-OMeTAD was employed for the thin film, the decay time was 68.7 ns, with an average decay time of 143.4 ns. In comparison, for the perovskite/**V1387** interface, a slightly slower decay time with τ_1 = 82.8 ns and an average decay time of τ = 227.5 ns were obtained. These results imply that **V1387**-based PSCs would exhibit a slightly lower or similar photovoltaic performance compared to that of spiro-OMeTAD-based PSCs.

Next, the solar cells were characterized under simulated solar illumination by measuring the current density as a function of the applied voltage ($J-V$ curves; see Figure 6a). The characteristic photovoltaic parameters of the PSCs with different HTMs were extracted from the $J-V$ scans and are reported in Table 3, where the results of the devices are arranged in order from lowest to highest PCE. All of the HTMs were doped with lithium bis(trifluoromethanesulfonyl)-imide (LiTFSI) in order to improve hole mobility. An analysis of the results suggests that the efficiency of the PSC decreases as the central core size of the HTM increases, since the PSCs with the HTMs that had bulkier TPA and carbazole core units (**V1389** and **V1391**, respectively) demonstrated the lowest PCE values. Conversely, out of all the new HTMs tested in PSCs, the best results were achieved with compounds that possessed the highest HOMO levels, **V1387** and **V1424**, which differ from one another only in the positions of the substitutions on the phenyl ring. However, this small structural variation between **V1387** and **V1424** results in an almost 1% difference in PCE, with **V1387** reaching a significantly high efficiency of 22.13%. In comparison, the benchmark HTM spiro-MeOTAD slightly outperformed the **V1387** devices

https://doi.org/10.1021/acs.chemmater.3c00708
Chem. Mater. 2023, 35, 5914−5923

Table 1. Thermal, Optical, and Photophysical Properties of the Synthesized Materials

ID	T_g (°C)[a]	T_{dec} (°C)[a]	λ_{abs} (nm)[b]	λ_{abs} (nm)[c]	I_p (eV)[d]	E_g (eV)[e]	μ_0 (cm^2 V^{-1} s^{-1})[f]
V1322	190	451	298, 376, 461	299, 379, 466	4.99	2.25	5.4×10^{-7}
V1387	209	452	297, 369	299, 372	4.92	2.82	8.5×10^{-7}
V1388	210	457	297, 367	299, 370	4.94	2.82	4.9×10^{-7}
V1389	231	455	299, 376, 451	298, 379, 454	5.03	2.38	1.3×10^{-6}
V1391	206	446	295, 375	293, 378	4.95	2.59	4.3×10^{-7}
V1424	203	445	298, 373	298, 375	4.89	2.64	1.9×10^{-6}

[a]The glass transition (T_g) and decomposition (T_{dec}) temperatures were determined by DSC and TGA, respectively (10 °C/min, N_2 atmosphere). [b]The absorption spectra were measured in a THF solution (10^{-4} M). [c]The absorption spectra were measured from thin films on glass substrates. [d]The HOMO energy levels of the thin films were measured using PESA. [e]The optical band gaps E_g were estimated from the edges of the electronic absorption spectra in the solid state. [f]The mobility values at zero field strength.

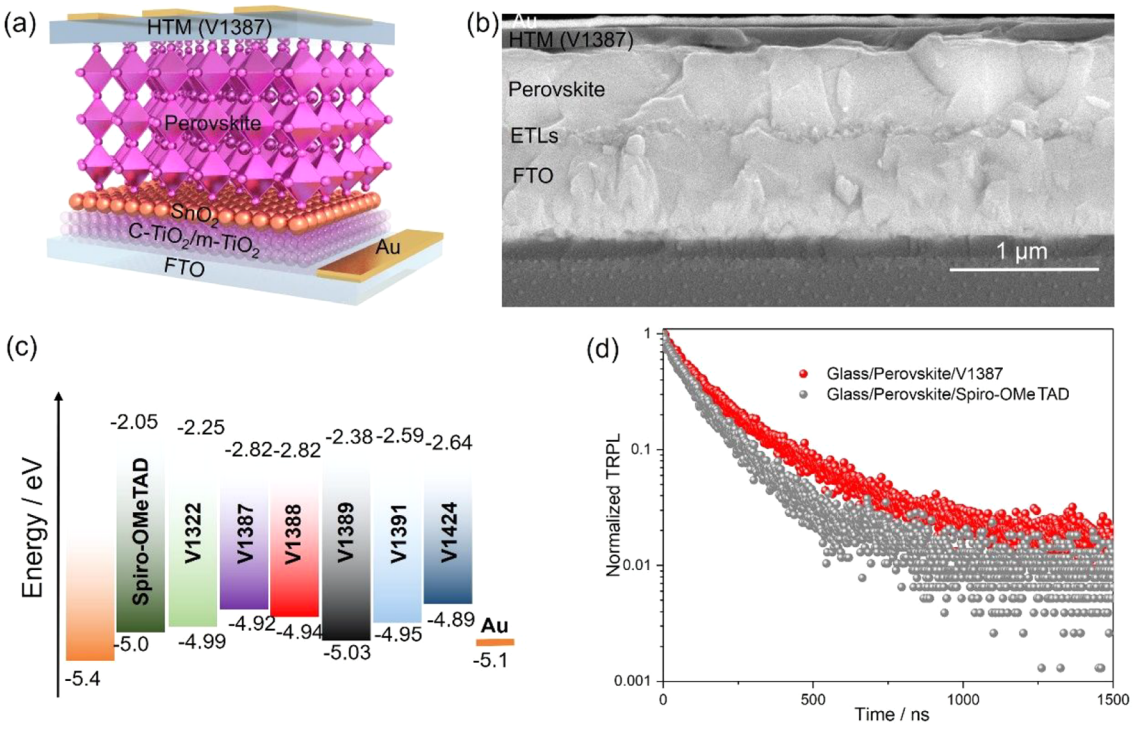

Figure 5. (a) A representative illustration of the structure of the fabricated PSCs. (b) A cross-sectional SEM image of the solar cell that used **V1387** as its HTM. (c) The energy levels of the various HTMs created in this study compared against sprio-OMeTAD and gold. (d) The TRPL measurements of a sample based on glass/perovskite/**V1387** (red) and of a sample based on glass/perovskite/spiro-OMeTAD (gray).

Table 2. Fitting Parameters of the Bi-Exponential Decay Function for TRPL Analysis of Glass/Perovskite Samples with Spiro-OMeTAD and V1387

films	fraction A_1 (%)	τ_1 (ns)	fraction A_2 (%)	τ_2 (ns)	average decay time, τ_{ave} (ns)[a]
FTO/perovskite/spiro-OMeTAD	61.1	68.7	38.9	186.7	143.4
FTO/perovskite/**V1387**	59.1	82.8	40.9	287.6	227.5

[a]The average decay time is calculated according to the equation $\tau_{ave} = (A_1\tau_1^2 + A_2\tau_2^2)/(A_1\tau_1 + A_2\tau_2)$.

(22.83%), delivering a PCE of 23.42% (Table S1, Figures 6b,c and S3). The *J*−*V* hysteresis of the champion PSCs can be observed in Figures 6b,c and S3. Low hysteresis indexes of 1.04 for **V1387**-based solar cells and 1.03 for spiro-OMeTAD-based solar cells were determined, which demonstrate the high quality of the fabricated PSCs. The steady state efficiencies were measured under AM1.5G illumination and are shown in Figure 6d. The devices based on spiro-OMeTAD and on **V1387** exhibit stable performances after 120 s output and show PCE values of 23.31% and 22.75%, respectively. It is clear that these values are extremely close to those obtained from the *J*−*V* curves. In addition, the incident photon to current efficiency (IPCE) of the devices based on **V1387** was determined to be 24.17 mA cm^{-2} (Figure S4), which is consistent with the short-circuit current (J_{sc}) values.

Maximum power point (MPP) tracking of the devices employing **V1387** and spiro-OMeTAD was compared under N_2 conditions (Figure 7a). Remarkably, the device with **V1387** retained 93.12% of its initial efficiency after a 1400 h output, whereas the device with spiro-OMeTAD maintained only 85.06% of the initial PCE under the same conditions. Figure 7b shows the T_{90} values of the stability of the devices. It can be

https://doi.org/10.1021/acs.chemmater.3c00708
Chem. Mater. 2023, 35, 5914−5923

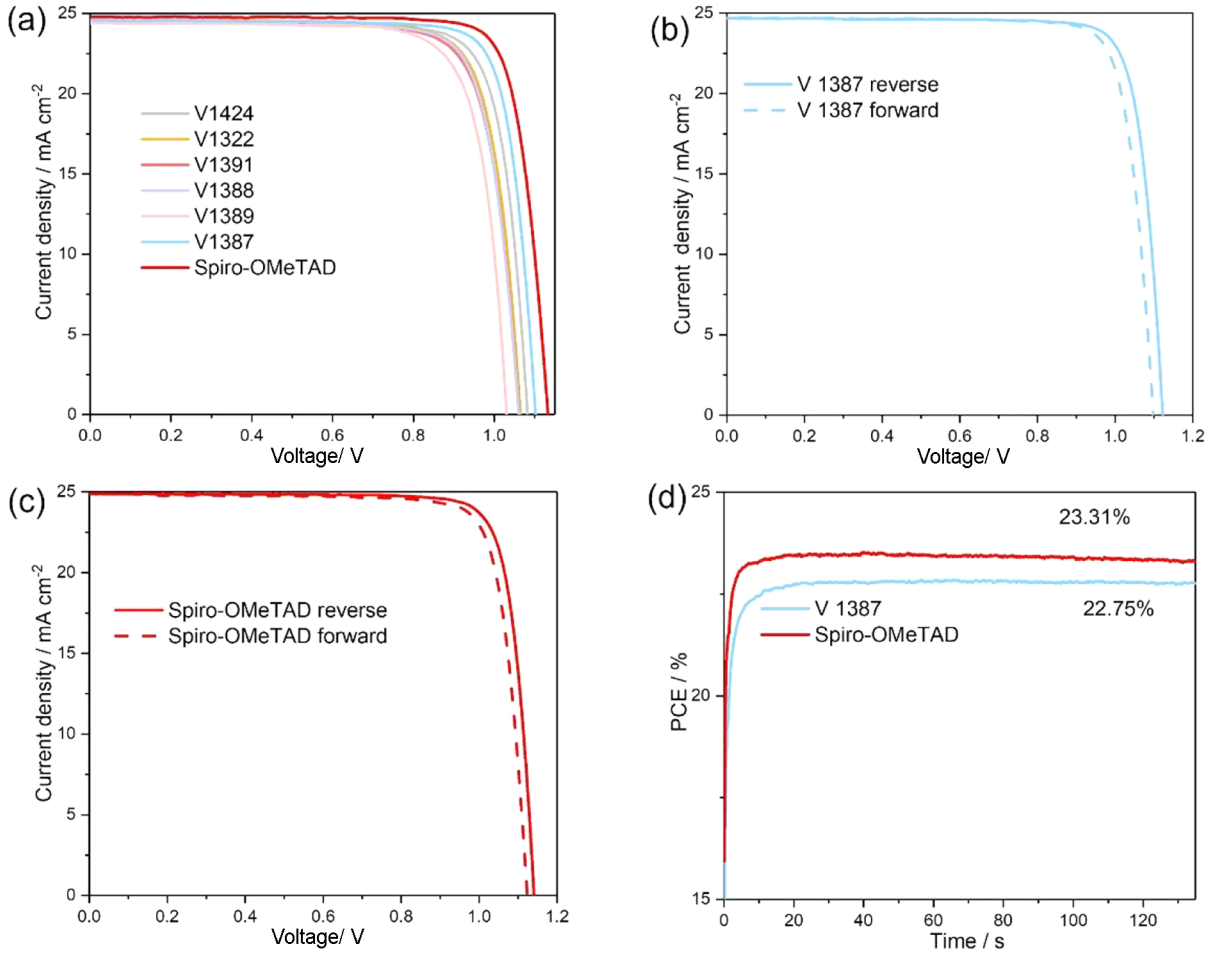

Figure 6. (a) $J-V$ curves of the PSCs based on the various HTMs. (b) Reverse and forward $J-V$ curves of the PSCs based on **V1387**. (c) Reverse and forward $J-V$ curves of the PSCs based on spiro-OMeTAD. (d) The steady state efficiencies of the champion PSCs based on spiro-OMeTAD (red) and **V1387** (blue).

Table 3. Photovoltaic Parameters Extracted from PSCs Based on the Various HTMs

HTMs	J_{sc} (mA cm^{-2})	V_{oc} (V)	fill factor, FF	PCE (%)
V1389	24.38	1.03	0.781	19.61
V1391	24.45	1.061	0.788	20.44
V1388	24.43	1.06	0.796	20.61
V1322	24.54	1.065	0.793	20.72
V1424	24.50	1.082	0.802	21.26
V1387	24.57	1.112	0.810	22.13
spiro-OMeTAD	24.79	1.133	0.813	22.83

seen that the device based on spiro-OMeTAD is less stable and reaches the T_{90} line quickly, in only 373 h. In addition, the **V1387**-based PSCs exhibit better ambient stability than devices based on spiro-OMeTAD (Figure 7c). Water contact angle (WCA) measurements reveal that the **V1387** film doped with LiTFSI exhibits a higher WCA (73°) than the spiro-OMeTAD-based films under the same conditions (68°). Hence, the greater hydrophobicity of **V1387** partially explains the high stability of the device that contains this HTM.

3. CONCLUSIONS

In this study, the synthesis and application of new HTMs that are composed of various central core units and substituted carbazole derivatives were developed in a facile two-step synthesis procedure. Their thermal, optical, and photoelectrical properties, as well as the PSC devices and interfacial transportation performances, were thoroughly investigated. All of the novel tested HTMs were successfully applied in PSCs, reaching an efficiency of up to 22.83%. Furthermore, the device employing the best performing HTM, **V1387**, demonstrated improved long-term stability compared to PSCs that used spiro-MeOTAD as a *p*-type organic charge carrier.

4. EXPERIMENTAL SECTION

4.1. Materials. Titanium diisopropoxide bis(acetylacetonate) (TAA), 4-*tert*-butylpyridine (*t*-BP), tin(IV) chloride pentahydrate ($SnCl_4$), bis(trifluoromethane) sulfonamide lithium salt (LiTFSI), FK209 [tris(2-(1*H*-pyrazol-1-yl)-4-*tert*-butylpyridine)-cobalt(III)-tris-(bis(trifluoromethylsulfonyl)imide)], chlorobenzene, dimethyl sulfoxide (DMSO), and dimethylformamide (DMF) were supplied from Sigma-Aldrich. Mesoporous TiO_2 (30-NRT), FAI, MAI, and MACl were purchased from GreatCell Solar. HAT6 and PbI_2 were purchased from TCI. Spiro-OMeTAD was purchased from Merck. All of the purchased chemicals were used as received without further purification.

4.2. Device Fabrication. For each device that was created, chemically etched FTO glass (Nippon Sheet Glass) was first cleaned with a detergent solution, deionized water, acetone, and isopropanol.

https://doi.org/10.1021/acs.chemmater.3c00708
Chem. Mater. 2023, 35, 5914−5923

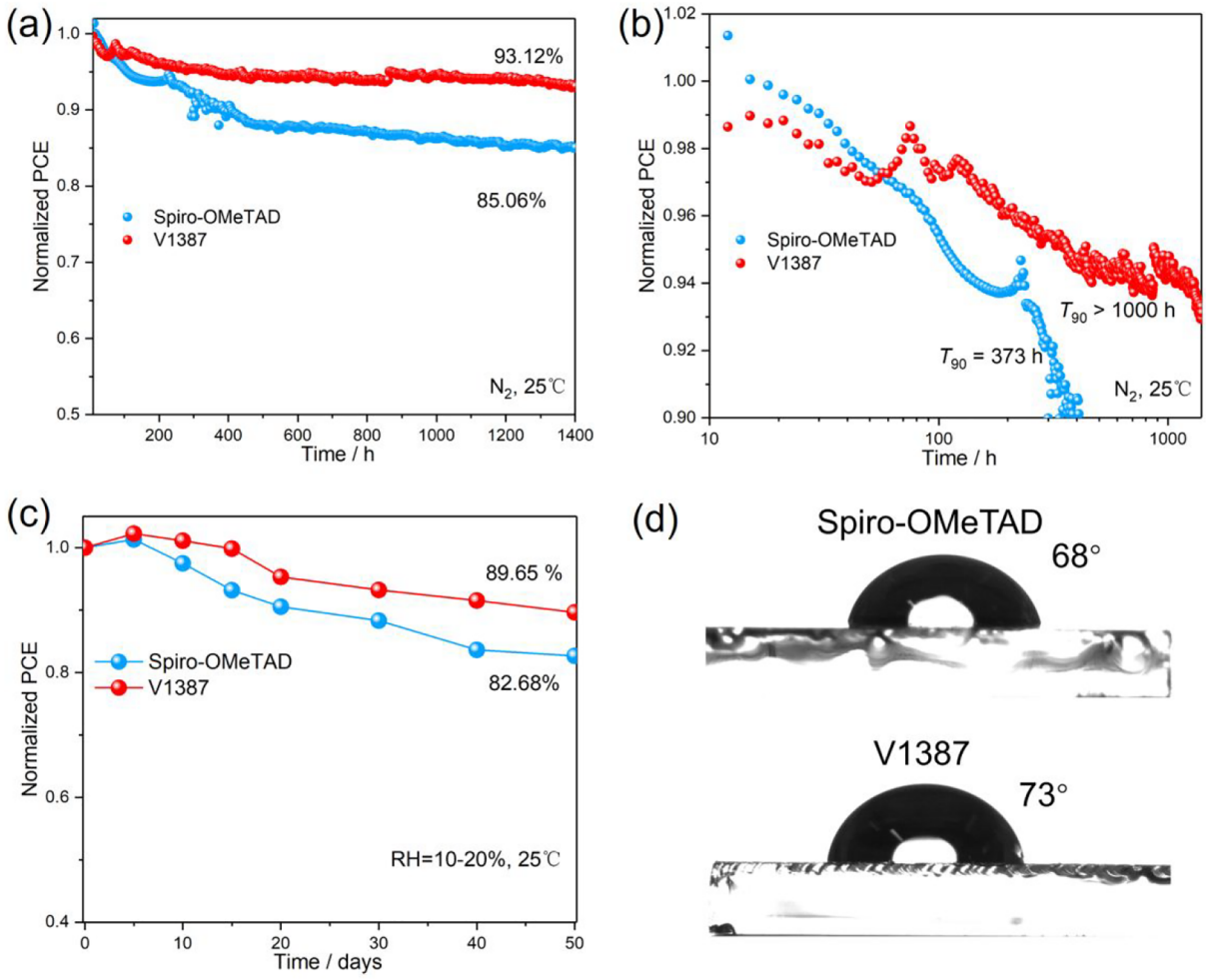

Figure 7. (a) MPP stability of the PSCs based on spiro-OMeTAD and **V1387** under the N_2 storage condition (25 °C). (b) T_{90} stability of the PSCs based on spiro-OMeTAD and **V1387**. (c) Ambient stability of the PSCs based on spiro-OMeTAD and **V1387**. (d) The contact angles of the spiro-OMeTAD and **V1387** films.

To create the compact TiO_2 (c-TiO_2) layer, a TAA solution in ethanol (1.2 mL of TAA in 20 mL of anhydrous isopropanol) was sprayed at 450 °C and was further heated for 1 h at 450 °C. Then, mesoporous TiO_2 (m-TiO_2) paste was diluted with ethanol with a ratio of 1:10, coated on top of the c-TiO_2 substrate at a speed of 3000 rpm for 20 s, and finally heated at 500 °C for 20 min. The tin oxide layer was formed by dissolving $SnCl_4$ in deionized water at a concentration of 12 μL/mL, spin-coating that solution on the mesoporous TiO_2 layer at a speed of 3000 rpm for 20 s, and heating the substrate at 190 °C for 60 min. Next, perovskite precursor solutions in DMSO/DMF 1:4 v/v (CsI = 11.78 mg; MAI = 11.12 mg; FAI = 228.72 mg; PbI_2 = 709.95 mg; MACl = 18.90 mg) were successively spin-coated onto the substrate at 1000 rpm for 10 s and 5000 rpm for 30 s, consecutively. Then, 200 μL of chlorobenzene was dropped on the substrate for 10 s at 5000 rpm, and the perovskite films were annealed at 150 °C for 10 min. The spiro-OMeTAD HTM solution was prepared by dissolving 80 mg of spiro-OMeTAD (Merck) in 1 mL of chlorobenzene. The novel HTMs of this study were prepared by dissolving 50 mg of each compound in 1 mL of chlorobenzene. The following additives were added: 18 μL of LiTFSI from the stock solution (520 mg in 1 mL of acetonitrile), 13 μL of FK209 [tris(2-(1*H*-pyrazol-1-yl)-4-*tert*-butylpyridine)-cobalt(III)-tris-(bis(trifluoromethylsulfonyl)imide)] (375 mg in 1 mL of acetonitrile), and 30 μL of 4-*tert*-butylpyridine. The HTM layer was formed by spin-coating the desired HTM solution at 4000 rpm for 20 s in order to achieve a thickness of 70 nm. Finally, deposition of the Au electrode completed the device. All of the preparative work done to deposit the perovskite and spiro-OMeTAD was carried out in a N_2-filled glovebox.

4.3. Device Characterization. The samples were prepared by spin-coating the HTM solution in chlorobenzene onto a FTO film (2000 rpm, 20 s); they were then irradiated by a 450 W Xe lamp filtered through a double monochromator (5 nm bandpass). The film morphology was investigated by using a high-resolution scanning electron microscope (SEM) (Merlin, Zeiss) that was equipped with a GEMINI II column and a Schottky field emission gun. Images were acquired with an in-lens secondary electron detector. For the PL lifetime measurements, samples were excited with a 408 nm pulsed laser (MDL 300, PicoQuant) with a 40 μm cm^2 pulse energy density. Current−voltage characteristics were recorded by applying an external potential bias to the cell while recording the generated photocurrent with a digital source meter (Keithley Model 2400). The light source was a 450 W Xe lamp (Oriel), equipped with a Schott K113 Tempax sunlight filter (Präzisions Glas & Optik GmbH) in order to match the emission spectrum of the lamp to the AM1.5G standard. Before each measurement, the exact light intensity was determined by using a calibrated Si reference diode that was equipped with an infrared cutoff filter (KG3, Schott). The cells were masked with an active area of 0.09 cm^2. Contact angle measurements were done with the help of a DSA30 drop shape analyzer instrument and analyzed with the help of the Krüss ADVANCE software.

4.4. Ionization Potential Measurements. The ionization potential was investigated by using the electron photoemission method, and the study was performed in air. The sample solutions

https://doi.org/10.1021/acs.chemmater.3c00708
Chem. Mater. 2023, 35, 5914−5923

(THF) were poured onto an aluminum-coated polyester film that was coated with an adhesive layer of a methyl methacrylate and methacrylic acid copolymer. A diffraction grating monochromator with a deuterium lamp was used for the experiment. The power of the falling light was ~5 × 10^{-8} W. A negative voltage (−100 V) was connected to the test sample. The electron photoemission current was measured with an open Geiger−Müller counter. The measurement method error was evaluated to be 0.03 eV.

4.5. Hole Drift Mobility Measurements. Carrier drift mobility was determined by the time-of-flight (XTOF) method. The material solution (THF) was poured onto aluminum-coated glass plates. The sample was poured from a solution of a pure substance, and the layers were dried for 1 h at 60 °C. The thickness of the transport layer was measured with an optical microscope-interferometer. The drift mobility of the holes (μ) was determined by using the electrophotographic mode with an electric field of (0.1/1) × 10^6 V/cm. Charge carriers were generated at the layer surface by illumination with a nitrogen laser using nanosecond pulses (λ = 337 nm). In most cases, the layers of pure material produced for the hole transport studies were of poor quality due to cracking and were not suitable for XTOF measurements due to rapid discharging. Therefore, charge transfer in layers of blends with bisphenol Z-polycarbonate (PC-Z), in weight ratios of 1:1, was used.

4.6. Study of Quantum Chemistry. Simulations of the ground state molecular structures for several of the most probable conformers were provided using Gaussian 16 software by means of density functional theory (DFT) via the B3LYP method and a 6-31G(d) basis set, supplemented with polarization functions (d). A list of several of the most probable molecular conformations is presented in Table S2. Two projections (*xy* and *xz*) of the mentioned conformations are presented in Figures S5−S10.

Electronic excitations were simulated using the semi-empirical TD method (for singlets). The parameters of the transition between MOs, which are related to the population of "spectroscopic" states, are presented in Table S3. Spatial distributions of the electron density for the HOMO−1, HOMO, LUMO, and LUMO+1 are presented in Tables S4−S6.

■ ASSOCIATED CONTENT

Supporting Information

The Supporting Information is available free of charge at https://pubs.acs.org/doi/10.1021/acs.chemmater.3c00708.

Detailed synthetic procedures, DSC and SEM data, detailed photovoltaic parameters, *J*−*V* curves, and results of the performed quantum chemistry studies (PDF)

■ AUTHOR INFORMATION

Corresponding Authors

Vytautas Getautis − *Department of Organic Chemistry, Kaunas University of Technology, Kaunas 50254, Lithuania;* orcid.org/0000-0001-7695-4677; Email: vytautas.getautis@ktu.lt

Mohammad Khaja Nazeeruddin − *Institute of Chemical Sciences and Engineering, École Polytechnique Federale de Lausanne (EPFL), Lausanne 1015, Switzerland;* orcid.org/0000-0001-5955-4786; Email: mdkhaja.nazeeruddin@epfl.ch

Authors

Aistė Jegorovė − *Department of Organic Chemistry, Kaunas University of Technology, Kaunas 50254, Lithuania*

Jianxing Xia − *Institute of Chemical Sciences and Engineering, École Polytechnique Federale de Lausanne (EPFL), Lausanne 1015, Switzerland*

Matas Steponaitis − *Department of Organic Chemistry, Kaunas University of Technology, Kaunas 50254, Lithuania*

Maryte Daskeviciene − *Department of Organic Chemistry, Kaunas University of Technology, Kaunas 50254, Lithuania*

Vygintas Jankauskas − *Institute of Chemical Physics, Vilnius University, Vilnius 10257, Lithuania*

Alytis Gruodis − *Institute of Chemical Physics, Vilnius University, Vilnius 10257, Lithuania*

Egidijus Kamarauskas − *Institute of Chemical Physics, Vilnius University, Vilnius 10257, Lithuania*

Tadas Malinauskas − *Department of Organic Chemistry, Kaunas University of Technology, Kaunas 50254, Lithuania;* orcid.org/0000-0002-5478-6550

Kasparas Rakstys − *Department of Organic Chemistry, Kaunas University of Technology, Kaunas 50254, Lithuania;* orcid.org/0000-0001-8016-9567

Khalid A. Alamry − *Chemistry Department, Faculty of Science, King Abdulaziz University, 21589 Jeddah, Saudi Arabia*

Complete contact information is available at: https://pubs.acs.org/10.1021/acs.chemmater.3c00708

Author Contributions

†A.J. and J.X. contributed equally to this work.

Notes

The authors declare no competing financial interest.

■ ACKNOWLEDGMENTS

This work has received funding from the European Regional Development Fund (Project 01.2.2-LMT-K-718-03-0040) under grant agreement with the Research Council of Lithuania (LMTLT) and from the Deputyship for Research & Innovation, Ministry of Education in Saudi Arabia, Project 526. Computations were performed on resources at the High Performance Computing Center, "HPC Saulėtekis" (Faculty of Physics, Vilnius University, Lithuania).

■ REFERENCES

(1) Rose, G. In *De novis quibusdam fossilibus quae in montibus Uraliis inveniuntur*; AG Schade, 1839; Chapters 3−5.

(2) Li, W.; Wang, Z.; Deschler, F.; Gao, S.; Friend, R. H.; Cheetham, A. K.; et al. Chemically diverse and multifunctional hybrid organic−inorganic perovskites. *Nat. Rev. Mater.* **2017**, *2*, 16099.

(3) Zhang, F.; Lu, H.; Tong, J.; Berry, J.; Beard, M. C.; Zhu, K. Advances in two-dimensional organic−inorganic hybrid perovskites. *Energy Environ. Sci.* **2020**, *13*, 1154.

(4) Gao, Y.; Pan, Y.; Zhou, F.; Niu, G.; Yan, C. Lead-free halide perovskites: a review of the structure−property relationship and applications in light emitting devices and radiation detectors. *J. Mater. Chem. A* **2021**, *9*, 11931.

(5) Ye, H. Y.; et al. Metal-free three-dimensional perovskite ferroelectrics. *Science.* **2018**, *361*, 151.

(6) Xiang, W.; Tress, W. Review on Recent Progress of All-Inorganic Metal Halide Perovskites and Solar Cells. *Adv. Mater.* **2019**, *31*, 1902851.

(7) Grancini, G.; Nazeeruddin, M. K. Dimensional tailoring of hybrid perovskites for photovoltaics. *Nat. Rev. Mater.* **2019**, *4*, 4.

(8) Yin, W. J.; Shi, T.; Yan, Y. Unique Properties of Halide Perovskites as Possible Origins of the Superior Solar Cell Performance. *Adv. Mater.* **2014**, *26*, 4653.

(9) Chen, Q.; De Marco, N.; Yang, Y.; Song, T.-B.; Chen, C.-C.; Zhao, H.; Hong, Z.; Zhou, H.; Yang, Y. Under the spotlight: The organic−inorganic hybrid halide perovskite for optoelectronic applications. *Nano Today.* **2015**, *10*, 355.

(10) Li, H.; Zuo, C.; Scully, A. D; Angmo, D.; Yang, J.; Gao, M. Recent progress towards roll-to-roll manufacturing of perovskite solar cells using slot-die processing. *Flex. Print. Electron.* **2020**, *5*, 014006.

(11) Taylor, A. D.; Sun, Q.; Goetz, K. P.; An, Q.; Schramm, T.; Hofstetter, Y.; Litterst, M.; Paulus, F.; Vaynzof, Y.; et al. A general approach to high-efficiency perovskite solar cells by any antisolvent. *Nat. Commun.* **2021**, *12*, 1878.
(12) Schackmar, F.; Eggers, H.; Frericks, M.; Richards, B. S.; Lemmer, U.; Hernandez-Sosa, G.; Paetzold, U. W. Perovskite Solar Cells with All-Inkjet-Printed Absorber and Charge Transport Layers. *Adv. Mater. Technol.* **2021**, *6*, 2000271.
(13) Babaei, A.; Zanoni, K. P. S.; Gil-Escrig, L.; Pérez-del-Rey, D.; Boix, P. P.; Sessolo, M.; Bolink, H. J. Efficient Vacuum Deposited P-I-N Perovskite Solar Cells by Front Contact Optimization. *Frontiers in chemistry.* **2020**, *7*, 936.
(14) Khenkin, M. V.; Katz, E. A.; Abate, A.; et al. Consensus statement for stability assessment and reporting for perovskite photovoltaics based on ISOS procedures. *Nat. Energy.* **2020**, *5*, 35.
(15) Xu, K.; Al-Ashouri, A.; Peng, Z. W.; et al. Slot-Die Coated Triple-Halide Perovskites for Efficient and Scalable Perovskite/Silicon Tandem Solar Cells. *ACS Energy Lett.* **2022**, *7*, 3600.
(16) Yoo, J. J.; Seo, G.; Chua, M. R.; et al. Efficient perovskite solar cells via improved carrier management. *Nature.* **2021**, *590*, 587.
(17) Pham, H. D.; Xianqiang, L.; Li, W.; Manzhos, S.; Kyaw, A. K. K.; Sonar, P. Organic interfacial materials for perovskite-based optoelectronic devices. *Energy Environ. Sci.* **2019**, *12*, 1177.
(18) Pham, H. D.; Yang, T. C. J.; Jain, S. M.; Wilson, G. J.; Sonar, P. Development of Dopant-Free Organic Hole Transporting Materials for Perovskite Solar Cells. *Adv. Energy Mater.* **2020**, *10*, 1903326.
(19) Yin, X.; He, Y.; Wang, X.; Wu, Z.; Pang, E.; Xu, J.; Wang, J. Recent Advances in Thermally Activated Delayed Fluorescent Polymer—Molecular Designing Strategies. *Front. Chem.* **2020**, *8*, 1.
(20) Kasparavicius, E.; Magomedov, A.; Malinauskas, T.; Getautis, V. Long-Term Stability of the Oxidized Hole-Transporting Materials used in Perovskite Solar Cells. *Chem. Eur. J.* **2018**, *24*, 9910.
(21) Magomedov, A.; Kasparavičius, E.; Rakstys, K.; Paek, S.; Gasilova, N.; Genevičius, K.; Juška, G.; Malinauskas, T.; Nazeeruddin, M. K.; Getautis, V. Pyridination of hole transporting material in perovskite solar cells questions the long-term stability. *J. Mater. Chem. C* **2018**, *6*, 8874.
(22) Meng, L.; You, J.; Yang, Y. Addressing the stability issue of perovskite solar cells for commercial applications. *Nat. Commun.* **2018**, *9*, 5265.
(23) Kasparavicius, E.; Franckevičius, M.; Malinauskiene, V.; Genevičius, K.; Getautis, V.; Malinauskas, T. Oxidized Spiro-OMeTAD: Investigation of Stability in Contact with Various Perovskite Compositions. *ACS Appl. Energy Mater.* **2021**, *4*, 13696.
(24) Bi, D.; Sun, L.; Grätzel, M.; Hagfeldt, A.; Gao, P.; Xu, B. Facile synthesized organic hole transporting material for perovskite solar cell with efficiency of 19.8%. *Nano Energy.* **2016**, *23*, 138.
(25) Xu, B.; Zhu, Z.; Zhang, J.; Liu, H.; Chueh, C. C.; Li, X.; Jen, A. K. Y. 4-Tert-butylpyridine Free Organic Hole Transporting Materials for Stable and Efficient Planar Perovskite Solar Cells. *Adv. Energy Mater.* **2017**, *7*, 1700683.
(26) Saliba, M.; Orlandi, S.; Matsui, T.; et al. A molecularly engineered hole-transporting material for efficient perovskite solar cells. *Nat. Energy.* **2016**, *1*, 15017.
(27) Kranthiraja, K.; Park, S. H.; Kim, H.; Gunasekar, K.; Han, G.; Kim, B. J.; Kim, C. S.; Kim, S.; Lee, H.; Nishikubo, R.; Saeki, A.; Jin, S. H.; Song, M. Accomplishment of Multifunctional π-Conjugated Polymers by Regulating the Degree of Side-Chain Fluorination for Efficient Dopant-Free Ambient-Stable Perovskite Solar Cells and Organic Solar Cells. *ACS Appl. Mater. Interfaces.* **2017**, *9*, 36053.
(28) Matsui, T.; Petrikyte, I.; Malinauskas, T.; Domanski, K.; Daskeviciene, M.; Steponaitis, M.; Gratia, P.; Tress, W.; Correa-Baena, J. P.; Abate, A.; Hagfeldt, A.; Grätzel, M.; Nazeeruddin, M. K.; Getautis, V.; Saliba, M. Additive-Free Transparent Triarylamine-Based Polymeric Hole-Transport Materials for Stable Perovskite Solar Cells. *ChemSusChem.* **2016**, *9*, 2567.
(29) Valero, S.; Collavini, S.; Völker, S. F.; Saliba, M.; Tress, W. R.; Zakeeruddin, S. M.; Grätzel, M.; Delgado, J. L. Dopant-Free Hole-Transporting Polymers for Efficient and Stable Perovskite Solar Cells. *Macromolecules.* **2019**, *52*, 2243.
(30) Xu, Y.; Bu, T.; Li, M.; Qin, T.; Yin, C.; Wang, N.; Li, R.; Zhong, J.; Li, H.; Peng, Y.; Wang, J.; Xie, L.; Huang, W. Non-Conjugated Polymer as an Efficient Dopant-Free Hole-Transporting Material for Perovskite Solar Cells. *ChemSusChem* **2017**, *10*, 2578.
(31) Jeong, M.; Choi, I. W.; Yim, K.; et al. Large-area perovskite solar cells employing spiro-Naph hole transport material. *Nat. Photonics* **2022**, *16*, 119.
(32) Jeon, N. J.; Na, H.; Jung, E. H.; et al. A fluorene-terminated hole-transporting material for highly efficient and stable perovskite solar cells. *Nat. Energy* **2018**, *3*, 682.
(33) Hu, Z.; Fu, W.; Yan, L.; Miao, J.; Yu, H.; He, Y.; Goto, O.; Meng, H.; Chen, H.; Huang, W. Effects of heteroatom substitution in spiro-bifluorene hole transport materials. *Chem. Sci.* **2016**, *7*, 5007.
(34) Zhu, H.; Zhang, F.; Liu, X.; Sun, M.; Han, J.; You, J.; Wang, S.; Xiao, Y.; Li, X. Dopant-free hole-transport material with a tetraphenylethene core for efficient perovskite solar cells. *Energy Technol.* **2017**, *5*, 1257.
(35) Gratia, P.; Magomedov, A.; Malinauskas, T.; Daskeviciene, M.; Abate, A.; Ahmad, S.; Grätzel, M.; Getautis, V.; Nazeeruddin, M. K. A Methoxydiphenylamine-Substituted Carbazole Twin Derivative: An Efficient Hole-Transporting Material for Perovskite Solar Cells. *Angew. Chem.* **2015**, *54*, 11409.
(36) Rakstys, K.; Paek, S.; Drevilkauskaite, A.; Kanda, H.; Daskeviciute, S.; Shibayama, N.; Daskeviciene, M.; Gruodis, A.; Kamarauskas, E.; Jankauskas, V.; Getautis, V.; Nazeeruddin, M. K. Carbazole-Terminated Isomeric Hole-Transporting Materials for Perovskite Solar Cells. *ACS Appl. Mater. Interfaces.* **2020**, *12*, 19710.
(37) Malinauskas, T.; Saliba, M.; Matsui, T.; Daskeviciene, M.; Urnikaite, S.; Gratia, P.; Send, R.; Wonneberger, H.; Bruder, I.; Graetzel, M.; Getautis, V.; Nazeeruddin, M. K. Branched methoxydiphenylamine-substituted fluorene derivatives as hole transporting materials for high-performance perovskite solar cells. *Energy Environ. Sci.* **2016**, *9*, 1681.
(38) Chen, Z.; Li, H.; Zheng, X.; Zhang, Q.; Li, Z.; Hao, Y.; Fang, G. Low-Cost Carbazole-Based Hole-Transport Material for Highly Efficient Perovskite Solar Cells. *ChemSusChem.* **2017**, *10*, 3111.
(39) Liu, X. X.; Ding, X.; Ren, Y.; Yang, Y.; Ding, Y.; Liu, X. X.; Alsaedi, A.; Hayat, T.; Yao, J.; Dai, S. A star-shaped carbazole-based hole-transporting material with triphenylamine side arms for perovskite solar cells. *J. Mater. Chem. C* **2018**, *6*, 12912.
(40) Yu, W.; Yang, Q.; Zhang, J.; Tu, D.; Wang, X.; Liu, X.; Li, G.; Guo, X.; Li, C. Simple Is Best: A p-Phenylene Bridging Methoxydiphenylamine-Substituted Carbazole Hole Transporter for High-Performance Perovskite Solar Cells. *ACS Appl. Mater. Interfaces.* **2019**, *11*, 30065.
(41) Kang, M. S.; Sung, S. D.; Choi, I. T.; Kim, H.; Hong, M.; Kim, J.; Lee, W. I.; Kim, H. K. Novel Carbazole-Based Hole-Transporting Materials with Star-Shaped Chemical Structures for Perovskite-Sensitized Solar Cells. *ACS Appl. Mater. Interfaces.* **2015**, *7*, 22213.
(42) Lu, C.; Choi, I. T.; Kim, J.; Kim, H. K. Simple synthesis and molecular engineering of low-cost and star-shaped carbazole-based hole transporting materials for highly efficient perovskite solar cells. *J. Mater. Chem. A* **2017**, *5*, 20263.
(43) Wu, F.; Ji, Y.; Zhong, C.; Liu, Y.; Tan, L.; Zhu, L. Fluorine-substituted benzothiadiazole-based hole transport materials for highly efficient planar perovskite solar cells with a FF exceeding 80%. *Chem. Commun.* **2017**, *53*, 8719.
(44) Wu, F.; Shan, Y.; Qiao, J.; Zhong, C.; Wang, R.; Song, Q.; Zhu, L. Replacement of Biphenyl by Bipyridine Enabling Powerful Hole Transport Materials for Efficient Perovskite Solar Cells. *ChemSusChem.* **2017**, *10*, 3833.
(45) Li, D.; Shao, J. Y.; Li, Y. Y.; Li, Y. Y.; Deng, L. Y.; Zhong, Y. W.; Meng, Q. New hole transporting materials for planar perovskite solar cells. *Chem. Commun.* **2018**, *54*, 1651.
(46) Leijtens, T.; Ding, I. K.; Giovenzana, T.; Bloking, J. T.; McGehee, M. D.; Sellinger, A. Hole Transport Materials with Low

https://doi.org/10.1021/acs.chemmater.3c00708
Chem. Mater. 2023, 35, 5914−5923

Glass Transition Temperatures and High Solubility for Application in Solid-State Dye-Sensitized Solar Cells. *ACS Nano* **2012**, *6*, 1455.
(47) Frisch, M. J.; Trucks, G. W.; Schlegel, H. B.; Scuseria, G. E.; Robb, M. A.; Cheeseman, J. R.; Scalmani, G.; Barone, V.; Petersson, G. A.; Nakatsuji, H.; Li, X.; Caricato, M.; Marenich, A. V.; Bloino, J.; Janesko, B. G.; Gomperts, R.; Mennucci, B.; Hratchian, H. P.; Ortiz, J. V.; Izmaylov, A. F.; Sonnenberg, J. L.; Williams-Young, D.; Ding, F.; Lipparini, F.; Egidi, F.; Goings, J.; Peng, B.; Petrone, A.; Henderson, T.; Ranasinghe, D.; Zakrzewski, V. G.; Gao, J.; Rega, N.; Zheng, G.; Liang, W.; Hada, M.; Ehara, M.; Toyota, K.; Fukuda, R.; Hasegawa, J.; Ishida, M.; Nakajima, T.; Honda, Y.; Kitao, O.; Nakai, H.; Vreven, T.; Throssell, K.; Montgomery, J. A., Jr.; Peralta, J. E.; Ogliaro, F.; Bearpark, M. J.; Heyd, J. J.; Brothers, E. N.; Kudin, K. N.; Staroverov, V. N.; Keith, T. A.; Kobayashi, R.; Normand, J.; Raghavachari, K.; Rendell, A. P.; Burant, J. C.; Iyengar, S. S.; Tomasi, J.; Cossi, M.; Millam, J. M.; Klene, M.; Adamo, C.; Cammi, R.; Ochterski, J. W.; Martin, R. L.; Morokuma, K.; Farkas, O.; Foresman, J. B.; Fox, D. J. *Gaussian 16*, rev. C.01; Gaussian, Inc., Wallingford, CT, 2019.
(48) Rakstys, K.; Saliba, M.; Gao, P.; Gratia, P.; Kamarauskas, E.; Paek, S.; Jankauskas, V.; Nazeeruddin, M. K. Highly Efficient Perovskite Solar Cells Employing an Easily Attainable Bifluorenylidene-Based Hole-Transporting Material. *Angew. Chem., Int. Ed.* **2016**, *55*, 7464.
(49) Daskeviciute-Geguziene, S.; Zhang, Y.; Rakstys, K.; Kreiza, G.; Khan, S. B.; Kanda, H.; Paek, S.; Daskeviciene, M.; Kamarauskas, E.; Jankauskas, V.; Asiri, A. M.; Getautis, V.; Nazeeruddin, M. K. Green-Chemistry-Inspired Synthesis of Cyclobutane-Based Hole-Selective Materials for Highly Efficient Perovskite Solar Cells and Modules. *Angew. Chem., Int. Ed.* **2022**, *61*, 61.
(50) Jeong, M.; Choi, I. W.; Go, E. M.; Cho, Y.; Kim, M.; Lee, B.; Jeong, S.; Jo, Y.; Choi, H. W.; Lee, J.; Bae, J. H.; Kwak, S. K.; Kim, D. S.; Yang, C. Stable perovskite solar cells with efficiency exceeding 24.8% and 0.3-V voltage loss. *Science.* **2020**, *369*, 1615.

https://doi.org/10.1021/acs.chemmater.3c00708
Chem. Mater. 2023, 35, 5914−5923